ACS APPLIED MATERIALS & INTERFACES

www.acsami.org

Research Article

Doping-Free High-Performance Photovoltaic Effect in a WSe_2 Lateral *p-n* Homojunction Formed by Contact Engineering

Hai Yen Le Thi, Tien Dat Ngo, Nhat Anh Nguyen Phan, Hoseong Shin, Inayat Uddin, Venkatesan A, Chi-Te Liang, Nobuyuki Aoki, Won Jong Yoo, Kenji Watanabe, Takashi Taniguchi, and Gil-Ho Kim*

Cite This: https://doi.org/10.1021/acsami.3c05451

Read Online

ACCESS | Metrics & More | Article Recommendations | Supporting Information

ABSTRACT: Two-dimensional transition metal dichalcogenides (TMDs) are promising materials for semiconductor nanodevices owing to their flexibility, transparency, and appropriate band gaps. A variety of optoelectronic and electronic devices based on TMDs *p-n* diodes have been extensively investigated due to their unique advantages. However, improving their performance is challenging for commercial applications. In this study, we propose a facile and doping-free approach based on the contact engineering of a few-layer tungsten di-selenide to form a lateral *p-n* homojunction photovoltaic. By combining surface and edge contacts for *p-n* diode fabrication, the photovoltaic effect is achieved with a high fill factor of ≈0.64, a power conversion efficiency of up to ≈4.5%, and the highest external quantum efficiency with a value of ≈67.6%. The photoresponsivity reaches 283 mA/W, indicating excellent photodiode performance. These results demonstrate that our technique has great potential for application in next-generation optoelectronic devices.

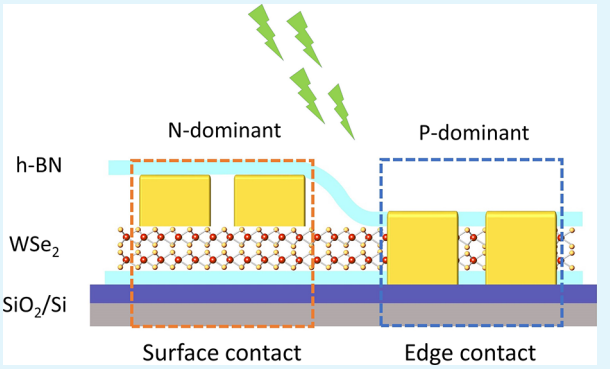

KEYWORDS: *WSe_2, edge contact, photovoltaic, WSe_2 diode, lateral p-n homojunction, WSe_2 photodiode*

INTRODUCTION

In recently reported TMDC devices, the utilization of lateral *p-n* junctions proves beneficial for increasing the shunt resistance and avoiding the electrical shorts in the device. Conversely, vertically stacked junctions are preferred for enhancing the absorption coefficient.[1] The resulting junction length is naturally shorter by employing a vertical configuration, where homojunction is formed using ultra-thin 2D TMDs. However, this shorter length restricts the attainment of significant photovoltaic effects, so generally lower open circuit voltage.[2] Furthermore, implementing the lateral configuration has proven advantageous for improving photovoltaic (PV) effects. A recent study by Zhang et al. highlighted the development of a lateral photodiode that achieved an open circuit voltage of 340 mV under 450 nm light illuminations. This notable achievement was primarily attributed to the lateral configuration, which facilitated the utilization of the entire channel for the photoresponse, leading to an efficient collection of photo-generated carriers.[3] This demonstration underscores the potential of lateral homojunctions to yield more significant PV effects than vertical ones.

For applications in devices such as photovoltaics, photodetectors, and light-emitting diodes, group III−V direct band gap semiconductors and bulk Si are widely used in conventional diode structures.[4−7] However, these materials lack flexibility and transparency and have low optical absorption coefficients, limiting their applications in flexible devices like solar cells or transparent displays.[8−11] Unlike ordinary semiconductors, there has been considerable interest in the utilization of two-dimensional (2D) layered materials, such as transition metal dichalcogenides (TMDs), for the fabrication of high-performance PV devices.[12−16] TMDs exhibit advantageous photovoltaic properties owing to their wide range of band gaps,[17] indicating the wavelengths of light that the materials can absorb and convert into energy.

Among TMDs, tungsten diselenide (WSe_2) has emerged as a potential candidate for an active material in optoelectronic devices due to its excellent properties such as ambipolar charge transport behavior,[18,19] high efficiency,[20−22] long lifetime,[23,24] and strong optical absorption.[25,26] Several methods have been reported for fabricating PV devices, including the utilization of vertical heterojunctions,[27,28] electrostatic gating,[29,30] and doping techniques.[31,32] However, most of these methods are complex to implement and result in defects and impurities at the semiconductor interface. Additionally, doped TMD-based

Received: April 20, 2023
Accepted: July 5, 2023

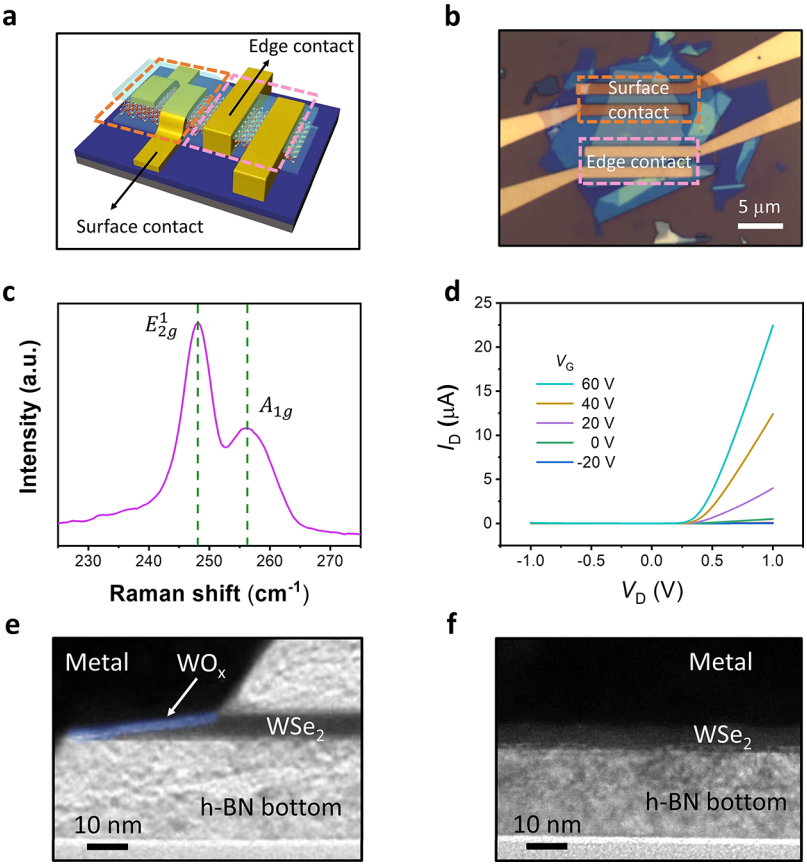

Figure 1. (a) Schematic diagram of a lateral WSe_2 PV device. (b) Optical microscopy image of the device. (c) Raman spectrum of WSe_2 flakes. (d) Diode characteristics of the WSe_2 PV device measured at different gate voltages. (e) and (f) HRTEM of cross-sectional edge and surface contacts, respectively, with the WO_x layer indicated in the edge contact device.

PV devices often experience severe degradation, which hinders the future application of TMDs in optoelectronic devices. Therefore, the development of the doping-free fabrication method and the enhancement of device stability are crucial for the advancement of TMD-based PV systems.

In this study, we fabricated a lateral WSe_2 PV device with the *p*-side realized by a self-formed amorphous oxide layer (WO_x) during the plasma etching process of edge contact fabrication, integrated with the n-side formed by surface contact. A significant challenge in achieving good p-type electrical surface contacts on WSe_2 is the Fermi-level pinning at the metal–semiconductor interface, which results in a high contact resistance regardless of the work function of metal work functions.[33,34] Moreover, the conventional surface-contacted device limits the scaling down of WSe_2-based FETs. Here, *p*-type characteristics are pronounced using edge contacts to overcome the aforementioned drawbacks,[35,36] and the surface contact device exhibits *n*-type behavior, leading to the demonstration of a WSe_2 homo-structure rectifying diode. The WSe_2 PV device exhibited high-performance photovoltaic characteristics without complicated doping methods. Our device displays a novel photovoltaic effect under visible light (520 nm). Specifically, a high fill factor (≈0.64), power conversion (≈4.5%), and external quantum efficiency (≈67.6%) were observed for our simple *p-n* homojunction. Moreover, excellent photoresponsivity of 283 mA/W was exhibited by our device. This promising photovoltaic effect induced by doping-free asymmetric contact architecture will facilitate the development of high-performance 2D solar cells and future electronic applications.

Figure 1a illustrates the schematic diagram of the lateral WSe_2 PV device, and in Figure 1b, an optical microscope image of the device is presented. A conventional dry transfer procedure was used to stack the WSe_2 (less than 10 nm thickness) on the selected bottom h-BN, and the In/Au metal electrodes were deposited on top of WSe_2 to form surface contacts that displayed *n*-type characteristics. Subsequently, the top h-BN was transferred to the metal electrodes and the sample was annealed with argon gas at 150 °C for 2 h to remove residues and bubbles. In order to expose the edges of WSe_2, a mixture of hexafluoride and oxygen (30/10 sccm) was used for the etching process with an etching time of 100 s. Finally, metallization of In/Au was performed to form edge contact electrodes with *p*-type features. A schematic of the fabrication process steps of the device is shown in Figure S1 in the Supporting Information. In Figure 1c, the Raman spectrum obtained using an excitation wavelength of 532 nm at 300 K is displayed to confirm that the material we used in this study is WSe_2, and the high-resolution transmission electron microscopy (HRTEM) image shows the number of layers of WSe_2 is ten layers. Two main vibrational modes were present: the E^1_{2g} peak (in-plane vibrational mode) located at ≈248 cm^{-1}, and the A_{1g} peak (out-of-plane vibrational mode) at ≈256 cm^{-1}. As shown in Figure 1d, we observed forward-rectification behavior at 300 K under a vacuum below 20 mTorr in the gate voltage range of $V_G = -20$ to 60 V, indicating that a *p-n* homojunction was generated after contact.[37] To further understand the

https://doi.org/10.1021/acsami.3c05451
ACS Appl. Mater. Interfaces XXXX, XXX, XXX−XXX

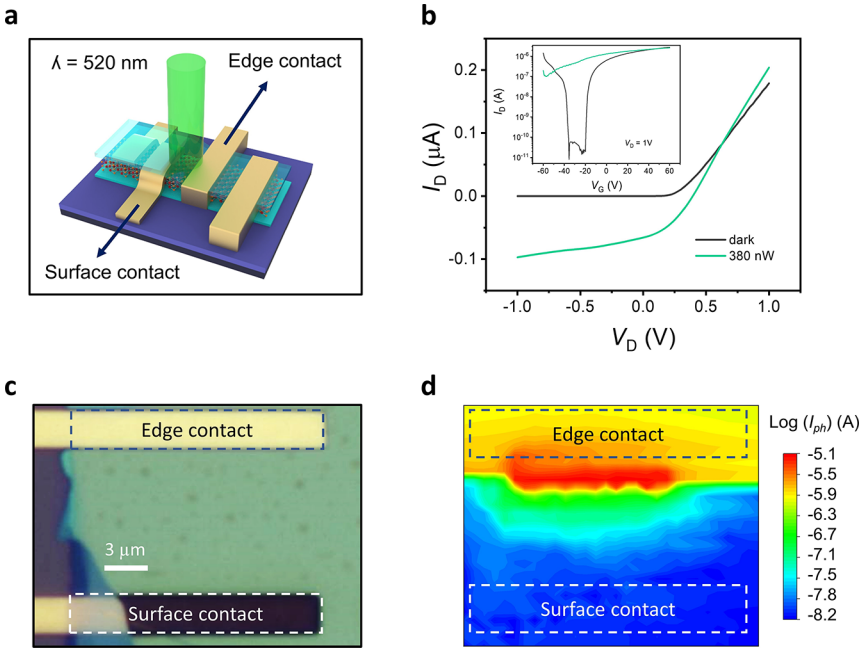

Figure 2. *I-V* characteristics of the lateral WSe_2 PV device and photocurrent mapping studies at 300 K. (a) Schematic of the WSe_2 PV device with a laser 520 nm. (b) Comparison of the output curves of the device measured in dark and laser illumination conditions. The inset represents the transfer curves of the device. (c) Optical microscope image of the WSe_2 PV used for photocurrent mapping. (d) Photocurrent mapping results of the *p-n*-WSe_2 diode scanned at V_G = 0 V and V_D = −1 V under the laser wavelength λ = 520 nm.

formation mechanism of our doping-free PV devices, we conducted cross-sectional HRTEM to examine the metal−semiconductor (MS) interface. According to Figure 1e, the HRTEM image at the MS interface of the edge contact indicates that an amorphous WO_x layer has formed between WSe_2 and metal, an observation that is consistent with our previous research.[35,38] This observation was further confirmed by energy-dispersive X-ray spectroscopy (EDS) mapping, as illustrated in Figure S2. The formation mechanism of the WO_x layer in the WSe_2 edge-contacted devices during the etching process is due to our ex-situ etching process, which enables oxygen from ambient binding with reactive dangling bonds from the exposed edge of WSe_2.[35] Additionally, we used an etching mixture containing O_2, which further stimulated the formation of the WO_x layer at the exposing edge. This has resulted in the WO_x layer being stably formed during the etching process, as a result of which WSe_2 edge contact devices are polarized *p*-type. The HRTEM image in Figure 1e reveals that the thickness of the WO_x layer measures approximately 3−4 nm, which is in relatively good agreement with our previously reported findings.[35] However, achieving precise control WO_x formation during the etching process remains challenging in our research. Therefore, this aspect presents a promising avenue for future investigations. It is worth noting that the thickness of the WO_x layer can impact the tunneling current at the edge contact. As the WO_x thickness increases, the tunneling resistance also increases, resulting in a degradation of the contact resistance.[35] In Figure 1f, the surface contact device demonstrates a smooth interface between the WSe_2 and the contact metal, with no observable damage or defects. This observation confirms the high-performance *n*-type characteristics of the surface contact device achieved in our research. The electrical performance of each device component is presented in Figure S3.

To understand the optoelectronic properties, the photocurrent of the device was measured using a 520 nm laser at different incident powers (P_{in}). P_{in} was calculated based on the equation $P_{in} = \frac{4A}{\pi d^2}P$ (A represents the working area of the device, d is the laser diameter, and P is the laser power).[39] All measurements were performed without the application of gate voltage. Figure 2a illustrates a schematic of the WSe_2 PV device with a laser 520 nm which was used to illuminate the homojunction device. To evaluate the photoresponse of the device, the output curves of the device are measured under dark and laser illumination conditions, as shown in Figure 2b. In order to confirm the increased photocurrent generation in the WSe_2 homojunction created from the WSe_2 edge contact, scanning photocurrent microscopy (SPCM) was performed in order to map the photocurrent flow. Figure 2c shows an optical microscope image of the *p-n* WSe_2 device used for scanning with white and blue rectangular boxes designed for the surface and edge electrode areas. The photocurrent mapping results for the *p-n* WSe_2 photodiode device illuminated under λ_{Laser} = 520 nm at V_D = −1 V and V_G = 0 V are shown in Figure 2d. The device shows a maximum response in the region close to the edge contact electrode; in contrast, we cannot observe a photoresponse near the surface contact region. The photocurrent generated from the individual surface and edge contacts device is shown in Figure S6. The output curves of both devices demonstrate that the photocurrent is not generated at a paired electrode of the edge and surface contacts. It is only generated at the *p-n* region close to the edge contact electrode.

In our homojunction WSe_2 *p-n* diode, *p*-dominance occurs due to the formation of the WO_x layer close to the edge contact electrodes. The thickness of the WO_x layer in our device was 3−4 nm; therefore, a *p-n* homojunction appeared near the edge contact instead of in the middle of the device, as shown in Figure 3a. The optoelectronic properties of the

https://doi.org/10.1021/acsami.3c05451
ACS Appl. Mater. Interfaces XXXX, XXX, XXX−XXX

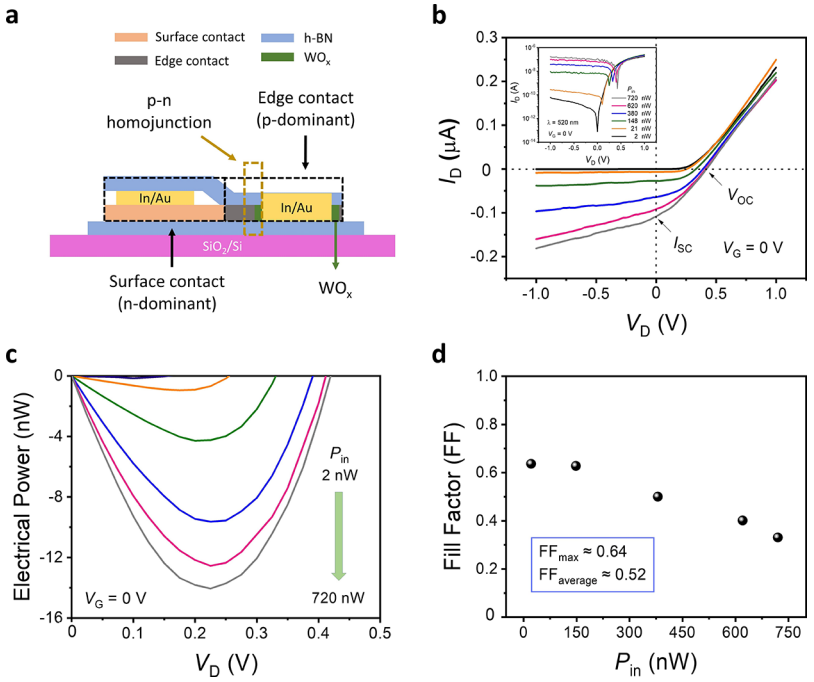

Figure 3. Optoelectronic properties were obtained with a 520 nm laser. (a) Explanation of the position of the *p-n* homojunction. (b) Photovoltaic effect of the WSe_2 *p-n* diode device at $V_G = 0$ V. (c) Electrical power P_{EL} with an incident laser power between 2 and 720 nW. (d) Plotting fill factor as a function of the incident laser power.

device were characterized by measuring the output characteristics I_D-V_D under a laser illumination with power varying from 2 to 720 nW, as shown in Figure 3b. The WSe_2 *p-n* diode exhibits a strong photovoltaic effect with both the short-circuit current (I_{SC}) and open-circuit voltage (V_{OC}) increase depending on the incident power increases because of the photogenerated carriers.[16,40,41] As the incident power is increased, the I_D-V_D curves are shifted toward more negative current values. From the output characteristics, the electrical power ($P_{EL} = V_{OC} \times I_{SC}$) is extracted and shown in Figure 3c that P_{EL} increases depending on the increase of the incident power with the maximum P_{EL} achieved at P_{in} = 720 nW. Figure 3d represents the fill factor (FF) (FF = $P_{EL,max}/I_{SC}V_{OC}$, where $P_{EL,max}$ is the maximum electrical power). The highest FF (FF_{max}) is ≈0.64, whereas the average FF ($FF_{average}$) is ≈0.52.

Figure 4a illustrates that when the gate voltage is positive ($V_G > 0$ V), the drain current level increases owing to the injection of more electrons in the conduction band of the In/WSe_2 surface contact (*n*-dominated). The transfer curve of the surface-contact device is shown in Figure S3c. However, a large hole current is observed when hole carriers are added to the WSe_2 channel, as shown in Figure 4b. This is caused by forming of a WO_x layer at the edge of WSe_2, resulting in the p-doping effect at negative gate voltage ($V_G < 0$ V). The transfer characteristics of the edge contact device are shown in Figure S3d. Figure 4c illustrates the energy band diagrams of the *p-n* homojunction-WSe_2, depicted under laser illumination, which can be used to understand the photocurrent properties. TMD materials undergo conduction band transitions when the laser energy exceeds the band gap, causing electrons to leave the valance band into the conduction band. Consequently, electron−hole pairs are formed by photon absorptions, which are then separated by the built-in electric field and an external drain bias (V_D). The number of electron−hole pairs that are recombined to produce a large photocurrent is controlled by this factor. As a result of laser illumination, electron−hole pairs are created near the depletion region. When the WSe_2 channel is changed with the self-formation of the WO_x layer at a junction, an increase in the photocurrent is observed by applying an external bias. This causes the photoexcited carriers to be pushed away from the junction in opposite directions.

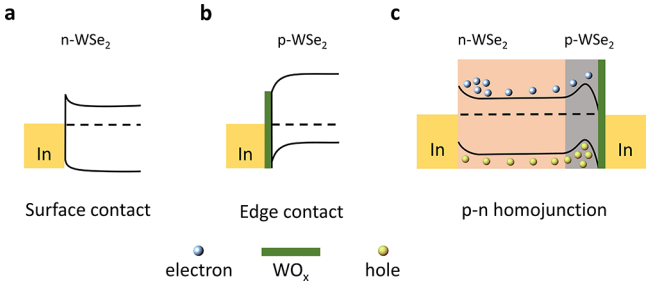

Figure 4. (a−c) Energy band alignment of *n*-WSe_2, *p*-WSe_2, and *p-n* homojunction-WSe_2, respectively.

A solar cell in its ideal configuration exhibits a linear relationship between I_{SC} and illumination power density (P), while a logarithmic relationship exists between V_{OC} and P, owing to the exponential shape of the *I-V* characteristic. As shown in Figure 5a, V_{OC} (left axis) and I_{SC} (right axis) are plotted as a function of the incident power derived from the I_D-V_D data, whereas I_{SC} follows a linear dependence on the power (linear fit, black line), whereas V_{OC} follows a logarithmic dependence (logarithmic fit, orange line). In the *p-n* configuration, the photocurrent generation is dominated by the photovoltaic effect, as shown in the good agreement between the experimental results and fitted curves (orange line, a linear fit to I_{SC}; black line, logarithmic fit to V_{OC}).

https://doi.org/10.1021/acsami.3c05451
ACS Appl. Mater. Interfaces XXXX, XXX, XXX−XXX

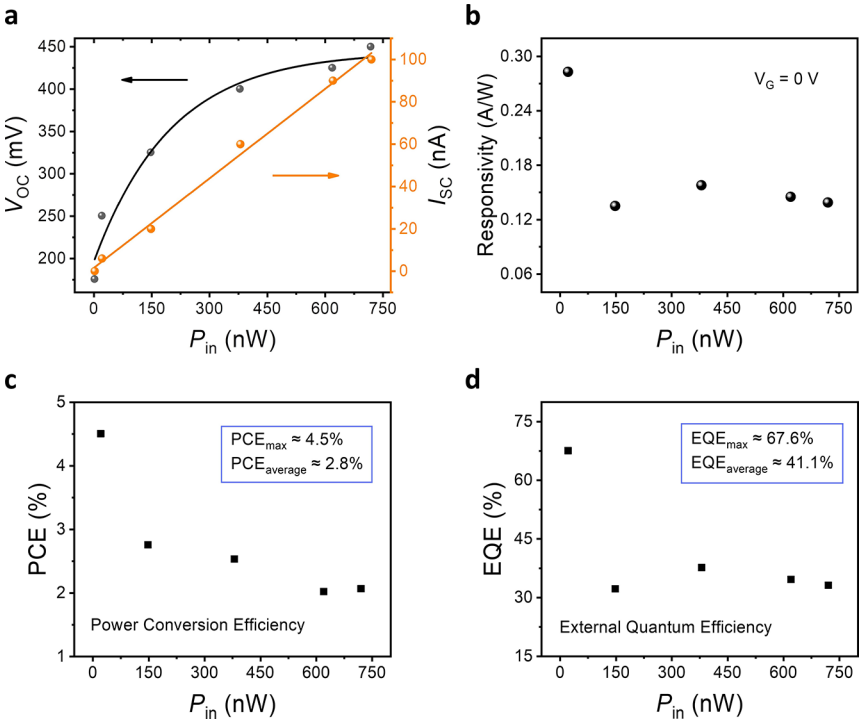

Figure 5. (a) Plot of open-circuit voltage (V_{OC}, left axis, black circles) and short-circuit current (I_{SC}, right axis, orange circles) as a function of incident power P_{in}. (b–d) Responsivity, power conversion efficiency, and external quantum efficiency as a function of laser power for local illumination at the WSe_2-source contact under V_D = 1 V and gate voltage V_G = 0 V, respectively.

Table 1. Performance Comparison of WSe_2 Lateral *p-n* Homojunction Photovoltaic Formed by Contact Engineering with Reported WSe_2 Photodetectors

device (method/structure)	illumination condition	FF	responsivity (mA/W)	detectivity (Jones)	response time	EQE (%)	PCE (%)	ref
WSe_2 (intrinsic)	532 nm	0.2	20			13	0.03	43
ReS_2/WSe_2 (heterojunction)	405 nm	0.56				15.3	1.5	27
p-n WSe_2 homojunction (O_2 plasma doping)	520 nm		250	7.7×10^9	41.8 ms	97		44
WSe_2 (O_2 plasma doping)	AM 1.5G	0.59					5.44	20
p-n WSe_2 homojunction (chemical doping)	520 nm		80	10^{11}	16 μs	20	1.4	15
WSe_2/Si (heterojunction)	white light (LED lamp)	0.55	86.11		23 ms		2.91	45
WSe_2 (chemical doping)	635 nm	0.4	468		4 ms	49.5	6.2	46
flexible WSe_2 solar cell (Gr/MoO_x contact)	AM 1.5G	0.61					5.1	47
homojunction WSe_2 *p-n* diode (doping-free)	520 nm	0.64	283	1.98×10^{10}	1.27 μs	67.6	4.5	this work

In order to assess the quality of the optoelectronic device, we calculated the responsivity (R), power conversion efficiency (PCE), and external quantum efficiency (EQE). To see the dependence of these values on the incident light power and calculate the average PCE and EQE, we plotted R, PCE, and EQE as a function of P_{in}. The responsivity was extracted by $R = I_{SC}/P_{in}$ with the maximum obtained responsivity value of about 283 mA/W at V_D = 1 V 520 nm laser power intensity wavelength. For the lowest incident power in Figure 5c, we calculated a PCE of ≈4.5% using the equation PCE = P_{EL}/P_{in}. In addition, we used the equation EQE = I_{SC}/P_{in} ($hc/e\lambda$) to calculate the EQE values, where h, c, and e are Planck's constant, the speed of light, and the electron charge, respectively. Figure 5d shows the EQE values as a function of the laser power, reaching a maximum value of 67.6% at P_{in} = 21 nW. As illustrated in Figure 5c,d, both the PCE and EQE values decrease as P_{in} increases. To explain this phenomenon, the responsivity is analyzed in relation to the laser power, as shown in Figure S11. The relationship between the responsivity and power density can be effectively described by the equation $R = \alpha P^{\beta - 1}$, where α = 0.0063 and β = 0.79 are constant values. When $|\beta - 1|$ approaches 1, the dominant mechanism at play is the photoconductive effect, and when $|\beta - 1|$ is smaller than 1, the dominant mechanism is the photogating effect.[42] Our result indicates that the $|\beta - 1|$ is equal to 0.213. Therefore, the photogating effect contributes to our finding (R and V_{OC} nonlinear dependence on P_{in}). Consequently, the increase in P_{in} results in a decrease in EQE and PCE.

Additionally, the photoresponse time was measured and presented in Figure S14a. Our device exhibited an exceptionally fast response, with a rising time of 1.27 μs and a falling

https://doi.org/10.1021/acsami.3c05451
ACS Appl. Mater. Interfaces XXXX, XXX, XXX−XXX

time of 1.65 μs was obtained. We also calculated the detectivity for our device by using the equation $D^* = R \times S^{1/2}/(2e \times I_{dark})^{1/2}$, where S represents the working area of the device (channel length L = 12.4 μm and channel width W = 4.2 μm). As depicted in Figure S14b, we achieved the highest detectivity of 1.98×10^{10} Jones at V_G = 0 V, V_D = 1 V, under a laser wavelength of 520 nm. Considering the equation $E = hc/\lambda$, it is evident that the WSe_2 multi-layer (with a band gap of approximately 1.35 eV) is capable of absorbing wavelengths up to 920 nm. Consequently, we anticipate that our device could exhibit enhanced performance and responsiveness under one-sun AM 1.5G illumination. This aspect represents a potential avenue for further exploration and expansion of our device's application in future studies.

To compare our fabricated WSe_2 lateral *p-n* homojunction, which was formed through contact engineering, with the existing literature, we have compiled the figures of merit in Table 1. The summarized results indicate that our device demonstrated consistent quality and relatively favorable parameters for a photodetector.

CONCLUSIONS

In conclusion, we successfully fabricated a WSe_2 homojunction-based diode capable of harnessing the photovoltaic effect without the need for complex doping or intricate fabrication methods. Our device exhibited remarkable photovoltaic performance when subjected to laser power illumination, surpassing recent reports in this field. SPCM analysis confirmed that the WSe_2 edge contact significantly contributed to the enhanced generation of photocurrent in response to laser power. Moreover, we achieved a high photoresponsivity of 283 mA/W at 21 nW. These findings demonstrate the potential of our simple architecture and its broad applicability to other 2D materials in future nano-integrated electronic and optoelectronic applications.

EXPERIMENTAL METHODS

Fabrication of the WSe_2 p-n Diode Device. The WSe_2 *n*-type bulk crystal (HQ graphene Inc.) was exfoliated using the traditional Scotch-tape method on a highly *p*-doped cleaned Si/SiO_2 substrate (285 nm). Raman spectroscopy was used to identify few-layer WSe_2 and h-BN flakes. Photolithography was performed to draw the outer electrodes pattern, followed by metal deposition using an electron-beam evaporator (Korea Vacuum Tech. KVT-2004). Later on, electron beam lithography was performed to draw the inner electrode pattern. The device was etched using a Mini-plasma System to make edge contacts in addition to surface contacts onto the WSe_2 channel. Immediately, the device was put into a deposition chamber to deposit metal layers of In (20 nm) and Au (30 nm) on the inner electrode pattern. Finally, the device was lift-off using acetone.

Characterization of the WSe_2 Device. To analyze the quality and surface of WSe_2 flakes, Raman spectroscopy was performed using a 532 nm laser under ambient conditions. The electrical and optical measurement of the device was performed using a Keithley 4200-SCS parameter analyzer under vacuum conditions below 20 mTorr in a dark environment connected to the probe station.

HRTEM and EDS at the Interface of the Metal−Semiconductor. In order to determine the cross-section of the edge contact and surface contact after fabrication, HRTEM images were obtained. To determine the doped elements in the samples, we performed EDS mapping and line scanning in addition to HRTEM images.

ASSOCIATED CONTENT

Supporting Information

The Supporting Information is available free of charge at https://pubs.acs.org/doi/10.1021/acsami.3c05451.

Sample preparation; experimental procedures; and supporting data (PDF)

AUTHOR INFORMATION

Corresponding Author

Gil-Ho Kim − *Sungkyunkwan Advanced Institute of Nano Technology (SAINT), Sungkyunkwan University (SKKU), Suwon 16419, Republic of Korea; Department of Electrical and Computer Engineering, Sungkyunkwan University (SKKU), Suwon 16419, Republic of Korea;* orcid.org/0000-0002-5153-4235; Email: ghkim@skku.edu

Authors

Hai Yen Le Thi − *Sungkyunkwan Advanced Institute of Nano Technology (SAINT), Sungkyunkwan University (SKKU), Suwon 16419, Republic of Korea*

Tien Dat Ngo − *Sungkyunkwan Advanced Institute of Nano Technology (SAINT), Sungkyunkwan University (SKKU), Suwon 16419, Republic of Korea*

Nhat Anh Nguyen Phan − *Department of Electrical and Computer Engineering, Sungkyunkwan University (SKKU), Suwon 16419, Republic of Korea*

Hoseong Shin − *Sungkyunkwan Advanced Institute of Nano Technology (SAINT), Sungkyunkwan University (SKKU), Suwon 16419, Republic of Korea*

Inayat Uddin − *Department of Electrical and Computer Engineering, Sungkyunkwan University (SKKU), Suwon 16419, Republic of Korea*

Venkatesan A − *Department of Electrical and Computer Engineering, Sungkyunkwan University (SKKU), Suwon 16419, Republic of Korea*

Chi-Te Liang − *Graduate Institute of Applied Physics, National Taiwan University, Taipei 106, Taiwan*

Nobuyuki Aoki − *Department of Materials Science, Chiba University, Chiba 263-8522, Japan;* orcid.org/0000-0001-9203-6040

Won Jong Yoo − *Sungkyunkwan Advanced Institute of Nano Technology (SAINT), Sungkyunkwan University (SKKU), Suwon 16419, Republic of Korea;* orcid.org/0000-0002-3767-7969

Kenji Watanabe − *Research Center for Functional Materials, National Institute for Materials Science, Tsukuba 305-0044, Japan;* orcid.org/0000-0003-3701-8119

Takashi Taniguchi − *International Center for Material Nanoarchitectonics, National Institute for Materials Science, Tsukuba 305-0044, Japan;* orcid.org/0000-0002-1467-3105

Complete contact information is available at: https://pubs.acs.org/10.1021/acsami.3c05451

Notes

The authors declare no competing financial interest.

ACKNOWLEDGMENTS

This work was supported by the National Research Foundation of Korea (NRF) grant funded by the Korean government (MSIT) (No. 2019R1A2C2088719 and 2021K2A9A2A08000168). N.A. acknowledges support from

the JSPS KAKENHI Grant Numbers 18H01812 and 21K18865, and Bilateral Joint Research Project between JSPS and NRF. K.W. and T.T. acknowledge support from JSPS KAKENHI (Grant Numbers 19H05790, 20H00354, and 21H05233) and A3 Foresight by JSPS.

REFERENCES

(1) Jariwala, D.; Davoyan, A. R.; Wong, J.; Atwater, H. A. Van Der Waals Materials for Atomically-Thin Photovoltaics: Promise and Outlook. *ACS Photonics* **2017**, *4*, 2962−2970.
(2) Du, J.; Liao, Q.; Liu, B.; Zhang, X.; Yu, H.; Ou, Y.; Xiao, J.; Kang, Z.; Si, H.; Zhang, Z.; Zhang, Y. Gate-Controlled Polarity-Reversible Photodiodes with Ambipolar 2D Semiconductors. *Adv. Funct. Mater.* **2021**, *31*, No. 2007559.
(3) Zhang, Y.; Ma, K.; Zhao, C.; Hong, W.; Nie, C.; Qiu, Z. J.; Wang, S. An Ultrafast WSe_2 Photodiode Based on a Lateral *p-i-n* Homojunction. *ACS Nano* **2021**, *15*, 4405−4415.
(4) Yoshikawa, K.; Kawasaki, H.; Yoshida, W.; Irie, T.; Konishi, K.; Nakano, K.; Uto, T.; Adachi, D.; Kanematsu, M.; Uzu, H.; Yamamoto, K. Silicon Heterojunction Solar Cell with Interdigitated Back Contacts for a Photoconversion Efficiency over 26%. *Nat. Energy* **2017**, *2*, 17032.
(5) Sim, Y. H.; Yun, M. J.; Lee, D. Y.; Cha, S. I. Application of a C-Si Solar Cell with a Three-Dimensional Structure to Indoor Photovoltaics. *Adv. Mater. Technol.* **2022**, *7*, No. 2101392.
(6) Cariou, R.; Benick, J.; Feldmann, F.; Höhn, O.; Hauser, H.; Beutel, P.; Razek, N.; Wimplinger, M.; Bläsi, B.; Lackner, D.; Hermle, M.; Siefer, G.; Glunz, S. W.; Bett, A. W.; Dimroth, F. III-V-on-Silicon Solar Cells Reaching 33% Photoconversion Efficiency in Two-Terminal Configuration. *Nat. Energy* **2018**, *3*, 326−333.
(7) Allen, T. G.; Bullock, J.; Yang, X.; Javey, A.; de Wolf, S. Passivating Contacts for Crystalline Silicon Solar Cells. *Nat. Energy* **2019**, *4*, 914−928.
(8) Taguchi, M.; Yano, A.; Tohoda, S.; Matsuyama, K.; Nakamura, Y.; Nishiwaki, T.; Fujita, K.; Maruyama, E. 24.7% Record Efficiency HIT Solar Cell on Thin Silicon Wafer. *IEEE J. Photovolt.* **2014**, *4*, 96−99.
(9) Zhang, Y.; Liu, Z.; Tadjer, M. J.; Sun, M.; Piedra, D.; Hatem, C.; Anderson, T. J.; Luna, L. E.; Nath, A.; Koehler, A. D.; Okumura, H.; Hu, J.; Zhang, X.; Gao, X.; Feigelson, B. N.; Hobart, K. D.; Palacios, T. Vertical GaN Junction Barrier Schottky Rectifiers by Selective Ion Implantation. *IEEE Electron Dev. Lett.* **2017**, *38*, 1097−1100.
(10) Kaltenbrunner, M.; Adam, G.; Głowacki, E. D.; Drack, M.; Schwödiauer, R.; Leonat, L.; Apaydin, D. H.; Groiss, H.; Scharber, M. C.; White, M. S.; Sariciftci, N. S.; Bauer, S. Flexible High Power-per-Weight Perovskite Solar Cells with Chromium Oxide-Metal Contacts for Improved Stability in Air. *Nat. Mater.* **2015**, *14*, 1032−1039.
(11) Xue, M.; Nazif, K. N.; Lyu, Z.; Jiang, J.; Lu, C. Y.; Lee, N.; Zang, K.; Chen, Y.; Zheng, T.; Kamins, T. I.; Brongersma, M. L.; Saraswat, K. C.; Harris, J. S. Free-Standing 2.7 Mm Thick Ultrathin Crystalline Silicon Solar Cell with Efficiency above 12.0%. *Nano Energy* **2020**, *70*, No. 104466.
(12) Sun, Z.; Martinez, A.; Wang, F. Optical Modulators with 2D Layered Materials. *Nat. Photonics* **2016**, *10*, 227−238.
(13) Wang, X.; Wang, P.; Wang, J.; Hu, W.; Zhou, X.; Guo, N.; Huang, H.; Sun, S.; Shen, H.; Lin, T.; Tang, M.; Liao, L.; Jiang, A.; Sun, J.; Meng, X.; Chen, X.; Lu, W.; Chu, J. Ultrasensitive and Broadband MoS_2 Photodetector Driven by Ferroelectrics. *Adv. Mater.* **2015**, *27*, 6575−6581.
(14) Hong, X.; Kim, J.; Shi, S. F.; Zhang, Y.; Jin, C.; Sun, Y.; Tongay, S.; Wu, J.; Zhang, Y.; Wang, F. Ultrafast Charge Transfer in Atomically Thin MoS2/WS2 Heterostructures. *Nat. Nanotechnol.* **2014**, *9*, 682−686.
(15) Tang, Y.; Wang, Z.; Wang, P.; Wu, F.; Wang, Y.; Chen, Y.; Wang, H.; Peng, M.; Shan, C.; Zhu, Z.; Qin, S.; Hu, W. WSe_2 Photovoltaic Device Based on Intramolecular p−n Junction. *Small* **2019**, *15*, No. 1805545.
(16) Furchi, M. M.; Pospischil, A.; Libisch, F.; Burgdörfer, J.; Mueller, T. Photovoltaic Effect in an Electrically Tunable Van Der Waals Heterojunction. *Nano Lett.* **2014**, *14*, 4785−4791.
(17) Wang, L.; Huang, L.; Tan, W. C.; Feng, X.; Chen, L.; Huang, X.; Ang, K. W. 2D Photovoltaic Devices: Progress and Prospects. *Small Methods* **2018**, *2*, No. 1700294.
(18) Wang, Z.; Li, Q.; Chen, Y.; Cui, B.; Li, Y.; Besenbacher, F.; Dong, M. The Ambipolar Transport Behavior of WSe_2 Transistors and Its Analogue Circuits. *NPG Asia Mater.* **2018**, *10*, 703−712.
(19) Lee, I.; Rathi, S.; Lim, D.; Li, L.; Park, J.; Lee, Y.; Yi, K. S.; Dhakal, K. P.; Kim, J.; Lee, C.; Lee, G. H.; Kim, Y. D.; Hone, J.; Yun, S. J.; Youn, D. H.; Kim, G. H. Gate-Tunable Hole and Electron Carrier Transport in Atomically Thin Dual-Channel WSe_2/MoS_2 Heterostructure for Ambipolar Field-Effect Transistors. *Adv. Mater.* **2016**, *28*, 9519−9525.
(20) Kim, K. H.; Andreev, M.; Choi, S.; Shim, J.; Ahn, H.; Lynch, J.; Lee, T.; Lee, J.; Nazif, K. N.; Kumar, A.; Kumar, P.; Choo, H.; Jariwala, D.; Saraswat, K. C.; Park, J. H. High-Efficiency WSe_2 Photovoltaic Devices with Electron-Selective Contacts. *ACS Nano* **2022**, *16*, 8827−8836.
(21) Sun, J.; Wang, Y.; Guo, S.; Wan, B.; Dong, L.; Gu, Y.; Song, C.; Pan, C.; Zhang, Q.; Gu, L.; Pan, F.; Zhang, J. Lateral 2D WSe_2 *p−n* Homojunction Formed by Efficient Charge-Carrier-Type Modulation for High-Performance Optoelectronics. *Adv. Mater.* **2020**, *32*, No. e1906499.
(22) Liu, B.; Zhang, X.; Du, J.; Xiao, J.; Yu, H.; Hong, M.; Gao, L.; Ou, Y.; Kang, Z.; Liao, Q.; Zhang, Z.; Zhang, Y. Synergistic-Engineered van Der Waals Photodiodes with High Efficiency. *InfoMat* **2022**, *4*, No. e12282.
(23) Tang, Y.; Mak, K. F.; Shan, J. Long Valley Lifetime of Dark Excitons in Single-Layer WSe_2. *Nat. Commun.* **2019**, *10*, 4047.
(24) Ersfeld, M.; Volmer, F.; Rathmann, L.; Kotewitz, L.; Heithoff, M.; Lohmann, M.; Yang, B.; Watanabe, K.; Taniguchi, T.; Bartels, L.; Shi, J.; Stampfer, C.; Beschoten, B. Unveiling Valley Lifetimes of Free Charge Carriers in Monolayer WSe_2. *Nano Lett.* **2020**, *20*, 3147−3154.
(25) Shen, Z.; Zhu, H.; Hong, J.; Gui, X.; Guan, H.; Dong, J.; Li, H.; Wang, X.; Qiu, W.; Zhang, E.; Ou, Y.; Lu, D.; Luo, L.; Lu, H.; Zhu, W.; Yu, J.; Luo, Y.; Chen, Z.; Peng, G. All-Optical Tuning of Light in WSe_2-Coated Microfiber. *Nanoscale Res. Lett.* **2019**, *14*, 353.
(26) Liu, H.; Zhu, X.; Sun, X.; Zhu, C.; Huang, W.; Zhang, X.; Zheng, B.; Zou, Z.; Luo, Z.; Wang, X.; Li, D.; Pan, A. Self-Powered Broad-Band Photodetectors Based on Vertically Stacked WSe_2/Bi_2Te_3 p-n Heterojunctions. *ACS Nano* **2019**, *13*, 13573−13580.
(27) Park, C.; Duong, N. T.; Bang, S.; Nguyen, D. A.; Oh, H. M.; Jeong, M. S. Photovoltaic Effect in a Few-Layer ReS_2/WSe_2 Heterostructure. *Nanoscale* **2018**, *10*, 20306−20312.
(28) Cho, A. J.; Song, M. K.; Kang, D. W.; Kwon, J. Y. Two-Dimensional WSe_2/MoS_2 p-n Heterojunction-Based Transparent Photovoltaic Cell and Its Performance Enhancement by Fluoropolymer Passivation. *ACS Appl. Mater. Interfaces* **2018**, *10*, 35972−35977.
(29) Ghosh, S.; Varghese, A.; Thakar, K.; Dhara, S.; Lodha, S. Enhanced Responsivity and Detectivity of Fast WSe_2 Phototransistor Using Electrostatically Tunable In-Plane Lateral p-n Homojunction. *Nat. Commun.* **2021**, *12*, 3336.
(30) Buscema, M.; Groenendijk, D. J.; Steele, G. A.; van der Zant, H. S. J.; Castellanos-Gomez, A. Photovoltaic Effect in Few-Layer Black Phosphorus PN Junctions Defined by Local Electrostatic Gating. *Nat. Commun.* **2014**, *5*, 4651.
(31) Ngo, T. D.; Lee, M.; Yang, Z.; Ali, F.; Moon, I.; Yoo, W. J. Control of the Schottky Barrier and Contact Resistance at Metal−WSe_2 Interfaces by Polymeric Doping. *Adv. Electron. Mater.* **2020**, *6*, No. 2000616.
(32) Pang, C. S.; Hung, T. Y. T.; Khosravi, A.; Addou, R.; Wang, Q.; Kim, M. J.; Wallace, R. M.; Chen, Z. Atomically Controlled Tunable Doping in High-Performance WSe_2 Devices. *Adv. Electron. Mater.* **2020**, *6*, No. 1901304.

https://doi.org/10.1021/acsami.3c05451
ACS Appl. Mater. Interfaces XXXX, XXX, XXX−XXX

(33) Liu, X.; Choi, M. S.; Hwang, E.; Yoo, W. J.; Sun, J. Fermi Level Pinning Dependent 2D Semiconductor Devices: Challenges and Prospects. *Adv. Mater.* **2022**, *34*, No. 2108425.
(34) Allain, A.; Kis, A. Electron and Hole Mobilities in Single-Layer WSe_2. *ACS Nano* **2014**, *8*, 7180−7185.
(35) Ngo, T. D.; Choi, M. S.; Lee, M.; Ali, F.; Yoo, W. J. Anomalously Persistent P-Type Behavior of WSe_2 Field-Effect Transistors by Oxidized Edge-Induced Fermi-Level Pinning. *J. Mater. Chem. C* **2022**, *10*, 846−853.
(36) Abuzaid, H.; Cheng, Z.; Li, G.; Cao, L.; Franklin, A. D. Unanticipated Polarity Shift in Edge-Contacted Tungsten-Based 2D Transition Metal Dichalcogenide Transistors. *IEEE Electron Dev. Lett.* **2021**, *42*, 1563−1566.
(37) Xia, H.; Luo, M.; Wang, W.; Wang, H.; Li, T.; Wang, Z.; Xu, H.; Chen, Y.; Zhou, Y.; Wang, F.; Xie, R.; Wang, P.; Hu, W.; Lu, W. Pristine PN Junction toward Atomic Layer Devices. *Light Sci. Appl.* **2022**, *11*, 170.
(38) Le Thi, H. Y.; Ngo, T. D.; Phan, N. A. N.; Yoo, W. J.; Watanabe, K.; Taniguchi, T.; Aoki, N.; Bird, J. P.; Kim, G. H. Self-Forming p−n Junction Diode Realized with WSe_2 Surface and Edge Dual Contacts. *Small* **2022**, *18*, No. e2204547.
(39) Island, J. O.; Blanter, S. I.; Buscema, M.; van der Zant, H. S. J.; Castellanos-Gomez, A. Gate Controlled Photocurrent Generation Mechanisms in High-Gain In_2Se_3 Phototransistors. *Nano Lett.* **2015**, *15*, 7853−7858.
(40) Baugher, B. W. H.; Churchill, H. O. H.; Yang, Y.; Jarillo-Herrero, P. Optoelectronic Devices Based on Electrically Tunable P-n Diodes in a Monolayer Dichalcogenide. *Nat. Nanotechnol.* **2014**, *9*, 262−267.
(41) Pospischil, A.; Furchi, M. M.; Mueller, T. Solar-Energy Conversion and Light Emission in an Atomic Monolayer p-n Diode. *Nat. Nanotechnol.* **2014**, *9*, 257−261.
(42) Zhang, W.; Huang, J. K.; Chen, C. H.; Chang, Y. H.; Cheng, Y. J.; Li, L. J. High-Gain Phototransistors Based on a CVD MoS_2 Monolayer. *Adv. Mater.* **2013**, *25*, 3456−3461.
(43) Ko, S.; Na, J.; Moon, Y. S.; Zschieschang, U.; Acharya, R.; Klauk, H.; Kim, G. T.; Burghard, M.; Kern, K. Few-Layer WSe2 Schottky Junction-Based Photovoltaic Devices through Site-Selective Dual Doping. *ACS Appl. Mater. Interfaces* **2017**, *9*, 42912−42918.
(44) Mitta, S. B.; Ali, F.; Yang, Z.; Moon, I.; Ahmed, F.; Yoo, T. J.; Lee, B. H.; Yoo, W. J. Gate-Modulated Ultrasensitive Visible and Near-Infrared Photodetection of Oxygen Plasma-Treated WSe_2 Lateral Pn-Homojunctions. *ACS Appl. Mater. Interfaces* **2020**, *12*, 23261−23271.
(45) Pataniya, P. M.; Zankat, C. K.; Tannarana, M.; Patel, A.; Narayan, S.; Solanki, G. K.; Patel, K. D.; Jha, P. K.; Pathak, V. M. Photovoltaic Activity of WSe_2/Si Hetero Junction. *Mater. Res. Bull.* **2019**, *120*, No. 110602.
(46) Yang, Y.; Huo, N.; Li, J. Gate-Tunable and High Optoelectronic Performance in Multilayer WSe_2 p-n Diode. *J. Mater. Chem. C* **2018**, *6*, 11673−11678.
(47) Nassiri Nazif, K.; Daus, A.; Hong, J.; Lee, N.; Vaziri, S.; Kumar, A.; Nitta, F.; Chen, M. E.; Kananian, S.; Islam, R.; Kim, K. H.; Park, J. H.; Poon, A. S. Y.; Brongersma, M. L.; Pop, E.; Saraswat, K. C. High-Specific-Power Flexible Transition Metal Dichalcogenide Solar Cells. *Nat. Commun.* **2021**, *12*, 7034.

https://doi.org/10.1021/acsami.3c05451
ACS Appl. Mater. Interfaces XXXX, XXX, XXX−XXX